Solid-liquid transition and rejuvenation similarities in complex flows of thixotropic materials studied by NMR and MRI

S. Rodts,[1] J. Boujlel,[1] B. Rabideau,[1] G. Ovarlez,[1] N. Roussel,[2] P. Moucheront,[1] C. Lanos,[3] F. Bertrand,[1] and P. Coussot[1,*]

[1]*Institut Navier, LMSGC, Université Paris-Est, 2 Allée Kepler, 77420 Champs sur Marne, France*

[2]*Laboratoire Central des Ponts et Chaussées, 58 Boulevard Lefebvre, 75732 Paris, France*

[3]*Laboratoire GCGM, INSA, Université Européenne de Bretagne, 20 Avenue des Buttes de Coesmes, CS 14315, 35043 Rennes, France*

(Received 24 June 2009; revised manuscript received 16 October 2009; published 4 February 2010)

We study the flow of a typical thixotropic material subjected to very different deformation histories (squeeze, shear, and extrusion) with either local (proton NMR and magnetic resonance imaging) or macroscopic measurements after different times of rest. Specifically, we measure the velocity fields and the spin-spin NMR relaxation of the material after different flow histories. The relaxation data exhibits a long relaxing component revealing information about the reversible microstructural evolution of the sample during aging-rejuvenation cycles. We show that for each deformation process, the evolution of the viscosity during the solid-liquid transition is similar by a factor related to the initial state of the material. Moreover, results examining the impact of the rate at which the deformation is imposed suggest that the state of the material during this transition may be described by a single parameter reflecting the average size and deformation of the material's flocs. These results also show that localization of flow occurs as a result of a progressive differential evolution of the material in different regions of the flow, and thus are determined by the boundary conditions of the flow.

DOI: 10.1103/PhysRevE.81.021402 PACS number(s): 82.70.−y, 83.60.La, 81.40.−z, 81.20.Hy

I. INTRODUCTION

Many materials, such as emulsions, foams, colloids, physical gels, etc., belong to the class of soft-jammed systems [1] or pastes, made of a high concentration of mesoscopic elements jammed in a volume of liquid and interacting via soft interactions. These soft interactions vary progressively with the distance between the elements [2]. One of the basic defining properties common to these materials is the existence of a yield stress, the critical stress beyond which the material changes from a solid to a liquid. These materials also show the tendency to age—in particular, at rest—as a result of progressive rearrangements due to thermal agitation coupled with soft interactions. Similarly, these materials also rejuvenate, particularly during flow, due to the disordering caused by deformation. Aging at rest is marked by the increase in the apparent yield stress (associated with the solid-liquid transition) and the shear modulus of the material with the duration of this rest (t_w). The aging properties of these materials in their solid regime have been shown to exhibit certain analogies with the properties of glasses [3]: elastic modulus vs time or stress vs deformation can be rescaled along single master curves after appropriate scaling for different times of rest, concentrations, or temperatures [4,5].

In contrast, little is known concerning the structural evolution during the opposite process—rejuvenation—which occurs when a material experiences a decrease in the apparent viscosity. Typically this phenomenon is observed when a stress larger than the yield stress is applied to a material which is initially at rest in its solid regime. A relatively progressive transition occurs from the solid to the steady-state liquid regime, during which the resulting shear rate, and thus the apparent viscosity of the system, decreases toward its steady-state value in the liquid regime [6]. For flocculated systems it is generally believed that rejuvenation has its origin in the progressive breakage of material into smaller and smaller flocs. At the solid-liquid transition the material breaks into just a few large solid flocs. As the deformation progresses, these flocs are then subdivided into a larger number of smaller blocks until equilibrium is achieved. It is believed that this process provides an increasing fraction of interstitial liquid which lubricates the relative motion of the flocs. Essentially the material is a suspension of flocs with a decreasing solid fraction, and thus has a decreasing apparent viscosity (see references in [7]).

Direct observations of the physical characteristics of the system at the local scale as it undergoes such an evolution, however, are scarce. One difficulty often encountered in these systems is that in conventional rheometer geometries (coaxial cylinders, parallel disks, cone and plate, etc.) shear banding often develops [8], an effect associated with strong rejuvenation in a specific region and aging in the rest of the material [9–11]. In such a case, the different regions of the materials evolve differently and can reach very different states. Such an effect is very difficult to detect from macroscopic measurements, which moreover cannot give an account of the different states and evolutions of the material in the different regions. Despite these challenges, recent work has provided direct observations of the material's destructuration in time during this solid-liquid transition, tending to confirm the decreasing floc size assumption [12].

For more than a decade, magnetic resonance imaging (MRI) [13] has proven to be a very versatile and powerful technique which can noninvasively provide relevant space resolved information about the structure and flow in complex fluids. Among its many possibilities, MRI can measure the local concentration of the solid phase within a paste, it can give local estimates of the velocity field in fluids, and—in some systems—it also turns out to be sensitive to microstruc-

*philippe.coussot@lcpc.fr

tural details. Different geometries can be designed for insertion into the MRI device, permitting *in situ* studies for the flow in complex systems. Commonly, simple rheometer geometries (Couette or cone and plate) [14–17] are used, usually for the purpose of a better characterization of basic rheological properties of a given system. A large variety of phenomena have been studied for a wide class of different materials using this unique combination of nuclear magnetic resonance (NMR) and rheometry (also called rheo-NMR): the molecular alignment in liquid crystals [18], migration and segregation in pastes and emulsions [11,16], yielding, and the critical shear rate and thixotropy in cements pastes [19], foams [20], and colloidal gels [21]. These studies have already led to important breakthroughs in the field of rheology (see, e.g., [11]). However, these experiments still consist of shearing a fluid along only one spatial dimension and could miss some typical three-dimensional (3D) characteristics of the fluid behavior.

Apart from the standard rheometrical setups, industrially applicable setups have also been successfully studied by MRI, such as screw extrusion devices [22,23] and a small concrete mixer [24]. These extremely complex induced flows, however, cannot be easily compared with theory or simulation, failing to provide any direct information about the rheological behavior of the material.

Currently, the study of ram extruders, in which the material flowing in a conduit is forced to flow through a conduit of smaller diameter, appears very promising. This geometry is an interesting compromise; the fluid is submitted to a real 3D flow in the vicinity of the die yet the flow geometry is still simple enough to compare the experimental results with computer simulation.

A number of studies have examined the extrusion of pastes by MRI. The extrusion of a hydrated Poly(tetrafluoroethylene) paste [25,26] was studied finding a drainage and a migration effect close to the die. Barnes *et al.* [27] looked at the time evolution of the velocity in certain regions of both a thixotropic mixture of polydimethylsiloxane (PDMS) with a commercial soap as well as a biscuit dough. Recently, we reported velocity fields for the extrusion of a homogeneous model yield stress fluid with varying ram velocity and die diameter, comparing these results with finite element simulation [28]. The advantage of studying these 3D flows is that it gives us an opportunity to test the 3D constitutive equations of complex fluids.

Apart from the MRI characterization of flows, nuclear magnetic resonance has also been used to characterize the microstructure of clay pastes. For example, it has been shown that the NMR spectroscopy and relaxometry of counterions as well as water diffusometry are able to detect the nematic ordering of clay particles [29,30]. More recently, it was shown that a combination of measuring the proton spin-lattice relaxation time and the signal intensity of water could provide a powerful means for determining the mass fraction in a bentonite paste for over five orders of magnitude [31]. Here, we study the solid-liquid transition of a thixotropic material in complex flows. In each case the material elements undergo significant deformation, so that at first approximation it can be assumed that the flow histories of the different regions within the material are all similar.

Under these conditions it is unlikely that the aforementioned problem of shear banding is able to develop. Thus, it can be assumed that the breakage of material into smaller and smaller flocs occurs—as a first approximation—homogeneously throughout the material. Examples of theses types of flows are the squeezing flows between two approaching parallel plates and orifice flows.

We performed extrusion experiments within our MRI setup. Using MRI and NMR observations of the velocity field and the sample itself, we show that the material rejuvenates as it approaches the die and that the velocity fields exhibit strong similarities for different ages of the material, suggesting that the material evolution from the solid to the liquid regime is similar regardless of its initial state. This result is supported by direct observations of the force vs deformation characteristics in squeeze flows, after different times of rest.

II. MATERIALS AND PROCEDURES

A. Material characteristics

For our tests we used a typical soft-jammed system which ages: a Na-bentonite suspension. Bentonite is a natural swelling clay composed of slightly flexible large aspect ratio particles. These particles tend to be penetrated by water, but can aggregate via edge-to-face links, such that the suspension can be viewed as a colloidal gel. In this context the aging, while at rest, may take its origin in a progression of the swelling, the aggregation process, or an evolution of the particle configuration. Each sample is prepared by strongly mixing the solid phase with water (volume fraction of clay particles in water: 3.9%). It is then left to rest for approximately 3 months before any test are performed. This avoids any further irreversible (chemical) aging over the duration of the experiments. The typical aging characteristics of the fluid are represented by an increase in the yield stress or the elastic modulus with the time of rest [5] or more generally an increase in the apparent viscosity (i.e., shear-stress–to–shear-rate ratio) of the fluid during a startup flow experiment.

We perform the latter type of test with our material (see Fig. 1). The sample is first loaded into a Couette geometry and presheared until it reaches a steady-state apparent viscosity. The material is then left to rest for a specified amount of time before it is subjected to a given apparent shear rate. This test is then repeated, loading a new sample into the geometry and following the entire procedure outlined above but with different times of rest.

In Fig. 1 we follow the shear stress vs time from the time the shear rate is imposed. These curves are shifted toward larger stress values for longer times of rest. Note that, in this test, the material is generally believed to undergo a transition from the solid regime to the liquid regime around the stress peak. The subsequent decrease in the stress beyond the peak is likely a result of the progressive rejuvenation of the material in the liquid regime as described in the Introduction.

B. MRI extrusion setup

NMR and MRI measurements were performed with a vertical 0.5 T proton MRI scanner (Bruker Avance 24/80 DBX)

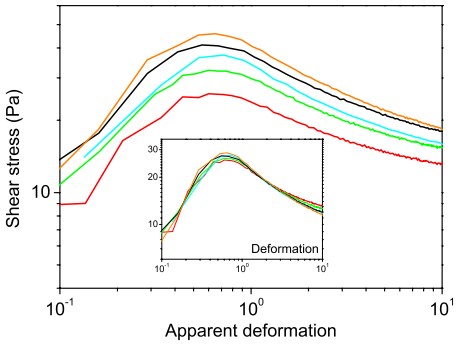

FIG. 1. (Color online) Shear stress vs apparent deformation in Couette flows under constant apparent shear rate (1.5 s^{-1}) with the bentonite suspension after different times of rest: (from bottom to top) 3, 10, 20, 30, and 60 min. The Couette geometry and the rheometer were described in [5,17]. The apparent deformation and shear rate were computed from the ratio of the relative motion of the tools to the gap. Inset: same data scaled by a stress factor (see values in Fig. 8) depending on the time of rest.

operating at 20 MHz. It is equipped with a birdcage rf coil (20 cm inner diameter) and a 3D gradient system (BGA26-Bruker) delivering a 50 mT/m gradient strength with a raising time of 500 μs.

The extrusion device consists of a large vertical syringe with an inner diameter of 80 mm and a length of 1540 mm. The piston of the syringe is driven by a load frame which was specifically designed to operate near the strong magnetic fields of the MRI scanner. Before each test the sample is first thoroughly mixed and then immediately poured inside the syringe. This ensures that, for each test, the material is in the same initial state. The bottom end of the syringe is then sealed with an axisymmetric cylindrical Poly(methyl methacrylate) (PMMA) die (10 mm in diameter). Tests are carried out by imposing a specified velocity to the piston, which can be varied from 0.1 μm/s to 10 mm/s, forcing the sample through the die. The syringe is made of a fiberglass composite material. It was designed for the use with very firm pastes and is built to withstand pressures of up to 2 MPa, the equivalent of 1 ton applied to the top of the sample. The entire setup is stiff enough to prevent local displacements exceeding 0.1 mm in any part of the setup due to mechanical stresses, even at the maximum load capacity. Only the lower region of the syringe reaches within the central core of the MRI magnet, where the measuring zone is delimited by the rf coil. Thus, results are limited to regions near the die entrance. As a result, the piston is normally absent from our measurements and is visible only at the very end of the extrusion experiments, when it is within a just a few centimeters from the die. A more thorough description of the setup is given in [28].

This work employed a few different MR techniques. MRI velocimetry was used to study the extrusion process, providing two-dimensional (2D) maps of the velocity components in vertical planes passing through the syringe. T_2-weighted imaging (see below) was used to detect migration effects in our samples. The aging of the material at rest was also characterized by means of NMR relaxation. The latter measurements were performed without the syringe system by placing a cylindrical glass container filled with approximately 1 l of the material within the scanner.

C. MRI velocimetry

The methodology for the MRI velocimetry consisted of a combination of a spin-echo–spin-warp imaging technique and a phase-encoded velocimetry [13]. The measurements were taken in a two-dimensional vertical slice passing through the syringe's central axis. Velocimetry experiments such as these consist of the measurement of a set of 2D MRI images in the same region of the sample, recorded as 2D scalar fields of complex values. Sensitivity to the local velocity components can be adjusted by introducing a space-dependent phase shift,

$$\Delta\phi(\mathbf{r}) = \alpha_x v_x(\mathbf{r}) + \alpha_y v_y(\mathbf{r}) + \alpha_z v_z(\mathbf{r}), \tag{1}$$

in which $\mathbf{r}$ is the spatial location, (v_x, v_y, v_z) are the local velocity components, and $(\alpha_x, \alpha_y, \alpha_z)$ are adjustable parameters which can be tuned by the operator before each experiment. When $(\alpha_x, \alpha_y, \alpha_z)$, known herein as encoding coefficients, are taken for each image, velocity components are then extracted by comparing the phases of each signal. In this work both the axial and radial components of the velocity were collected using three different sets of encoding coefficients.

Although MRI velocimetry relies primarily on standard methodology, special attention was taken to overcome a number of challenges. First, spin-warp imaging requires stable flow conditions. Although this is a plausible assumption within the syringe, this is certainly not the case at the exit of the die where the continuous extrusion flow begins to drip under the force of its own weight [32]. Using the spin-warp technique, this unsteady behavior not only creates a local blurring of the image, but also results in spatially oscillating artifacts which superimpose themselves upon the entire image, damaging the key information in the other sections of the sample. These oscillations are not isotropic; instead, they develop from the intermittent flow regions along only one of the spatial directions, known as the phase direction. The MRI scanner allows us to choose whether this direction is horizontal or vertical. We chose the horizontal (radial) direction as the phase direction. This choice precludes any interference of these artifacts with the regions of immediate interest to us, specifically the region just above the die entrance.

A second difficulty encountered was the weak signal-to-noise ratio (SNR) in our collected data, which limited the accuracy of the velocity measurements. This was particularly severe since the uncertainty of measurement is not a relative error but rather an absolute error. Since most of our measurements dealt with low ram velocities, i.e., less than 1 mm/s, they were prone to compete with the molecular diffusion of water. This challenge was overcome by using numerically optimized sets of encoding coefficients, which gave the optimum signal-to-noise ratio when determining the velocities. This optimization took into account disruptive phenomena such as the self-diffusion of water in bentonite and the small T_2 relaxation time (about 10 ms). This led us to work with

much larger values for the encoding coefficients than those usually recommended by current methodology [33]. The reconstruction of velocities maps from raw MRI measurements required the use of a 2D adaptation of the one-dimensional (1D) continuity-based reconstruction algorithm described in [24]. All of the velocity measurements used a slice thickness of 1 cm; a vertical and a horizontal field of view of 20 and 10 cm, respectively; and a pixel size of 2×2 mm. Approximately 40 min of flow were needed to obtain a complete velocity field. All of the measurements presented in this work concern a region which is centered slightly above the die entrance. The use of large encoding coefficients, while necessary for maintaining a good signal-to-noise ratio for the velocities, had the drawback of producing signal losses in strongly sheared regions of the flow, especially in the immediate vicinity of the die entrance. Thus, all of the data in this region and below, although visible in some of the images, are not relevant and should be disregarded. Measurements for the velocity field inside of the die using a different type of material may be found in [28].

D. NMR spin-spin relaxation and T_2-weighted imaging

1. NMR relaxation in heterogeneous systems

Spin-spin and spin-lattice relaxation rates of the hydrogen nuclei (proton) within water molecules are just a few of the numerous NMR properties which can be determined from the sample. They originate from both the magnetic interactions of proton spins with their surroundings and the time correlation properties of these interactions due to translational and rotational motions caused by the thermal agitation of water molecules [34]. They tell us certain things about the various physicochemical and microstructural aspects of the sample.

Typical relaxation experiments consist of exciting the entire sample in such a way that the water molecules emit a decaying NMR signal whose intensity $s(t)$ exhibits, in simple cases, a first-order exponential evolution, which at short times reflects the amount of water in the sample and follows the relations

$$s(t) \propto m_w \exp(-t/T_2) \quad \text{for spin-spin relaxation,} \tag{2a}$$

$$s(t) - s(t \to +\infty) \propto m_w \exp(-t/T_1) \quad \text{for spin-lattice relaxation,} \tag{2b}$$

where m_w is the total amount of water within the sample, and T_1 and T_2 are the spin-lattice and spin-spin relaxation times. In the case of heterogeneous materials, T_1 is sometimes preferred since the measurement of T_2 is prone to suffer bias from a number of sources, the most important of which is the irreversible defocusing of local NMR signals in the presence of internal magnetic field inhomogeneities [35,36]. In our working conditions (20 MHz), free unconfined water is found to have T_1 and T_2 relaxation times of around 3 s. In a water saturated bentonite sample, however, as well as many other porous materials, relaxation is found to be orders of magnitude shorter. Indeed, there are strong interactions of the water molecules with the solid phase of the sample. These interactions are mainly dipole-dipole magnetic interactions with paramagnetic species contained either as defects in the platelets' crystallography or as impurities (especially iron and manganese). The adsorption of water molecules onto the clay platelets and the nanoscale confinement of water between parallel platelets significantly modify the dynamics of the molecules.

For water embedded in biological cells Brownstein and Tarr [37] proposed a continuous model for water relaxation. Their model considers that during the relaxation process, the relaxing part $s(\mathbf{r},t)$ of the local NMR signal density emitted at a position $\mathbf{r}$ inside the sample evolves according to water diffusion and bulk relaxation.

Essentially, it models an enhanced relaxation process on the cell surface by means of a relaxivity coefficient, according to

$$\frac{\partial s}{\partial t} = D\Delta s - \frac{s}{T_{bulk}} \quad \text{(inside the pore)},$$
$$D\mathbf{n}\cdot\nabla s = \rho s \quad \text{(on the surface)}, \tag{3}$$

where $D \approx 2\times 10^{-9}$ m^2 s^{-1} is the self-diffusion coefficient of water molecules, T_{bulk} is the relaxation time of bulk water, ρ is the surface relaxivity, and $\mathbf{n}$ is the normal vector to the surface, directed toward the inside of the cell. In any finite-sized sample, this model appears to have a complete basis of normalized real-valued eigenmodes $\varphi_i(\mathbf{r})$ with eigenvalues of the relaxation times T_i. These make it possible to write the general solution of the relaxation problem as

$$s(t) = s_0 \sum_i \left[\int_{\vec{r}} \varphi_i(\mathbf{r}) dV\right]^2 \exp\left(-\frac{t}{T_i}\right), \tag{4}$$

where s_0 is the NMR signal density at the beginning of the experiment. This model was extended to the study of fluids embedded in suspensions and to fluids embedded in porous media. In porous and heterogeneous systems, multiexponential decays are observed [38]. Eigenmodes usually take significant values only within a close proximity to the individual pores, such that there is a characteristic relaxation time T_i involved in Eq. (4) for a given pore size R. These characteristic times are believed to obey the two asymptotical rules [37]:

$$\frac{1}{T_i} = \frac{1}{T_{bulk}} + \frac{\rho S}{V} \quad \text{if} \quad \frac{\rho R}{D} \ll 1, \tag{5a}$$

$$\frac{1}{T_i} = \frac{1}{T_{bulk}} + \text{const} \times \frac{D}{R^2} \quad \text{if} \quad \frac{\rho R}{D} \gg 1, \tag{5b}$$

where S/V corresponds to the local surface-to-volume ratio of the pore and is often interpreted as the inverse of the pore diameter. Equations (5a) and (5b) correspond to the surface limited and diffusion limited regimes as classified by Brownstein and Tarr. An experimental verification of the linear and quadratic dependences of relaxation time with the pore size was performed in [39] for a macroporous systems with a very good agreement.

For clay suspensions, however, water relaxation is often found to exhibit only a monoexponential-like behavior

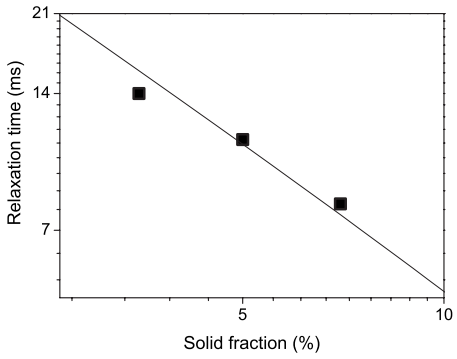

FIG. 2. T_2 as a function of solid volume fraction for a bentonite suspension (different from that used for all the other tests in this paper). The continuous line is a fit of Eq. (6).

[31,40]. Because most of the relevant microstructure of the sample is at the nanoscale, water diffusion is fast enough to sample all of the encountered relaxation sources during the relaxation process. Relaxation then occurs in the surface limited regime as defined by Brownstein and Tarr [37], and Eq. (3) reduces to only one significant eigenmode, which approaches a uniform value throughout the entire sample. The related relaxation time T is still expected to scale as the ratio of the volume of water to the fraction of the clay suspension's surface which is accessible to the water molecules. If the particle size distribution is fixed, the surface area is proportional to the solid (volume) fraction ϕ. With the water concentration being simply $1-\phi$, we finally get

$$\frac{1}{T}-\frac{1}{T_{bulk}}\propto\frac{\phi}{1-\phi}. \tag{6}$$

Thus, it turns out that T is primarily a function of the clay concentration.

In many practical situations $\phi<10\%$ and $T\ll T_{bulk}$, so that Eq. (6) can be approximated as

$$\frac{1}{T}\propto\phi. \tag{7}$$

Such a linear dependence was verified for the T_1 (spin-lattice) relaxation of a bentonite suspension by Ohkubo *et al.* [40] in the concentration range 2–300 % (by weight) and by Dvinskikh *et al.* [31] in the concentration range 0.001–20 % (by volume), confirming *a posteriori* the hypothesis of surface limited relaxation.

A best fit line of Eq. (6) along with the T_2 (spin-spin) measurements performed on a freshly mixed bentonite suspensions in the concentration range 3–7 % (by volume) is displayed in Fig. 2 and shows a good qualitative agreement. The samples used in these experiments were from a fresh batch of bentonite and were not the actual ones used in the experiments.

2. T_2-weighted imaging

To detect the presence of any phase migration or spatial variations in the clay concentration occurring during the extrusion process, the spatial distribution of spin-spin relaxation time T_2 was collected at different stages of the extrusion process. Observations were made in the same slices as those of the velocity measurements. We used T_2-weighted MRI, which consists of imaging the intensity of the NMR signal emitted from each pixel at a special time T_E (the echo time) throughout the relaxation process. For a monoexponential decay, the image intensity then scales as

$$I(r)\propto m(r)\exp[-T_E/T_2(r)], \tag{8}$$

where $m(r)$ and $T_2(r)$ are the local water concentration and relaxation time, respectively. Strictly speaking, the T_2-weighted MRI is also sensitive to $m(r)$; however, in our experiments $m(r)$ was not prone to undergo strong modifications because of the low initial volume fraction of bentonite particles. The optimal T_2 sensitivity is obtained when T_E roughly approaches (within −50% to +100%) a certain average value T_2 throughout the entire sample. We used a T_E of 15 ms which turned out to be well suited for the average relaxation time of our suspensions, which was measured to be approximately 10 ms.

3. Spin-Spin relaxation measurements

Unfortunately our T_2-weighted images had a rather low signal-to-noise ratio (SNR ~ 10) due to the short relaxation time of the samples. This prevented us from observing the kinetics of the entire relaxation process and left us unable to assess its monoexponential or multiexponential behavior. For further insight into the spin-spin relaxation process, independent experiments were performed in which all of the sample regions were measured together, producing one average relaxation curve with a high SNR.

To avoid measurement bias caused by any microheterogeneities present in the sample, we used a Carr-Purcell-Meiboom-Gill (CPMG) NMR sequence [35,41] which minimizes unwanted irreversible signal defocalization by periodically refocusing the NMR signal at the local scale throughout the relaxation process, thus producing a series of NMR echoes; the higher the refocusing frequency, the better the artifact compensation. In our experiments, the smallest achievable refocusing period within the limitations of the hardware was 1 ms. To validate our data, a series of experiments was performed with refocusing intervals of 1, 2, 4, and 8 ms, respectively. This test is shown in Fig. 3. The graphs show that there is actually very little influence of the refocusing interval, suggesting that in our measurements, an accurate bias compensation was always achieved. In the following, only the relaxation curves measured with a refocusing time of 1 ms are given.

III. EXTRUSION

A. Magnetic resonance imaging

Due to the axisymmetric flow, the 2D velocity fields presented here represent the typical velocity in the vertical axial plane. Typical velocity fields (given as the magnitude) obtained for our aging system are shown in Figs. 4(a) and 4(b). Due to our difficult working conditions, a signal loss is likely to occur in the vicinity of the die entrance or even inside the die. In such a situation, any flow velocity measured inside

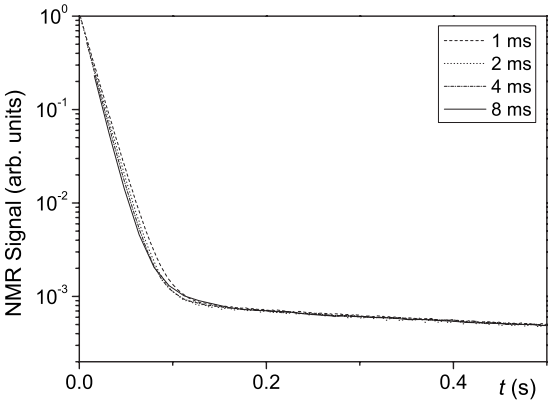

FIG. 3. Benchmark test for NMR CPMG measurements of spin-spin relaxation. Relaxation curves obtained on the same bentonite sample for refocusing times of 1, 2, 4, and 8 ms, respectively.

the die can be badly biased and should not be regarded (as mentioned before in Sec. II C). Since the material can age or rejuvenate during flow its behavior is time dependent and one might expect some time evolution of the flow characteristics. Our results show that there is in fact no significant evolution of the velocity field inside the syringe over the 40 min duration of the measurement. Indeed, as explained above, with the spin-warp MRI technique, unsteady flow conditions would result in a spreading of artifacts along the phase-encoding direction of the picture (i.e., the radial direction in the present work). In the upper wider zone of the setup, the well-defined sharp vertical edges of the velocity images are a strong indication that the flow is stable over the duration of the experiment. Moreover, considering the tendency of such fluids to shear localize we could have expected some kind of progressive breakage or fracture of more or less large regions. Once again the consistency of the velocity field proves that this is not the case. Breakage, if it occurs, is at a sufficiently small scale such that the continuum assumption remains valid at our scale of observation.

Typical T_2-weighted images of the samples are shown in Fig. 5. Note the presence of a large air bubble along the ram face in Fig. 5(b), taken at the end of the experiment. It is highly unlikely that this bubble originated from an air leakage between the ram and the inner wall of the syringe. During the experiment, there is a greater pressure within the syringe than outside the syringe making it more likely that the material be ejected from the syringe in the case of a leak. The dynamic seal between the ram and the syringe was held using four lobe rings. At the conclusion of the experiment both the ram and the syringe were found to be free of bentonite residue, supporting the lobe rings' capacity for holding a strong seal. We believe that it is much more likely that the air bubble originates from the paste itself, resulting from a progressive "harvesting" of small bubbles initially settled between the bentonite paste and the inner wall of the syringe. Since this large air bubble is elastic, it is possible that this could generate differences between the actual ram velocity and the upper fluid velocity. In each case it was independently verified that the velocity field far from the die always corresponded to the imposed ram velocity.

Our observations show that, within the uncertainty of our data, the velocity is nearly uniform far from the die and very close to the piston velocity, regardless of the apparent yield stress of the material (see Fig. 6). This implies that in the conduit, the shear is localized within a very thin region along the wall. This effect is typically expected for a yield stress fluid; however, the fact that we do not see any region of smaller velocity at the approach of the wall suggests that there could be some additional effects such as wall slip or shear banding as previously reported for such materials in simple shear [11]. Because almost all of the fluid far from the die is flowing as a plug, we can be confident that most of the fluid remains in its initial state (i.e., the state reached at the end of the rest period) before arriving to the flow region perturbed by the die entrance.

The velocity field becomes more complex at the approach of the die. There is a region of much lower velocity in the corner of the conduit. The shape of this region is roughly similar to that observed for a Newtonian or a yield stress fluid (in the usual range of Bingham numbers) (see Fig. 4). One might wonder whether this region corresponds to a region of lower velocities as is seen for a Newtonian fluid or if it is in fact a stopped fluid region (dead zone) as is seen for a true yield stress fluid. Our data make it possible to clarify that point. First of all, the extent of the dead zone is independent of the flow history. Specifically, flows occurring immediately after mixing and flows occurring after 30 h of rest have very similar shapes in this region. Moreover, after a flow following such a long time of rest one can see that this region becomes visible on a T_2-weighted image (see Fig. 5) when the piston approaches the die. The image intensity in the corners was found to be about 10–15 % less than that in the center of the conduit, halfway between the piston and the die. This difference may be explained (with regard to the sensitivity of T_2 to the clay concentration) by a relative increase in the clay concentration (10–15 %) in the corners. However, an attempt to quantitatively determine this concentration difference by recovering samples in the different regions and drying and weighing lacked the necessary precision to confirm this.

B. Spin-spin NMR relaxation

To confirm that the T_2 contrast observed in the MRI images corresponds to water migration away from these regions, or is instead due to changes in the sample microstructure, an independent experiment was carried out. It consisted of measuring the entire spin-spin NMR signal decay of a well-mixed bentonite suspension after different times of rest as it was left to age for up to 72 h. In such an experiment, no clay migration can occur, and only the effects of aging upon the sample are observed. Each CPMG measurement lasted for approximately 10 min. When compared with the duration of the entire experiment, this can be viewed as an instantaneous snapshot of the sample properties. The measurements discussed herein used a refocusing time of 1 ms. It was verified that they were not impaired with any significant experimental bias, following the procedure given in Sec. II D.

Following the initial stirring and after each resting time we observe that the signal decay is clearly not monoexponential (see Fig. 7), but can instead be very well described by the two-component relaxation process,

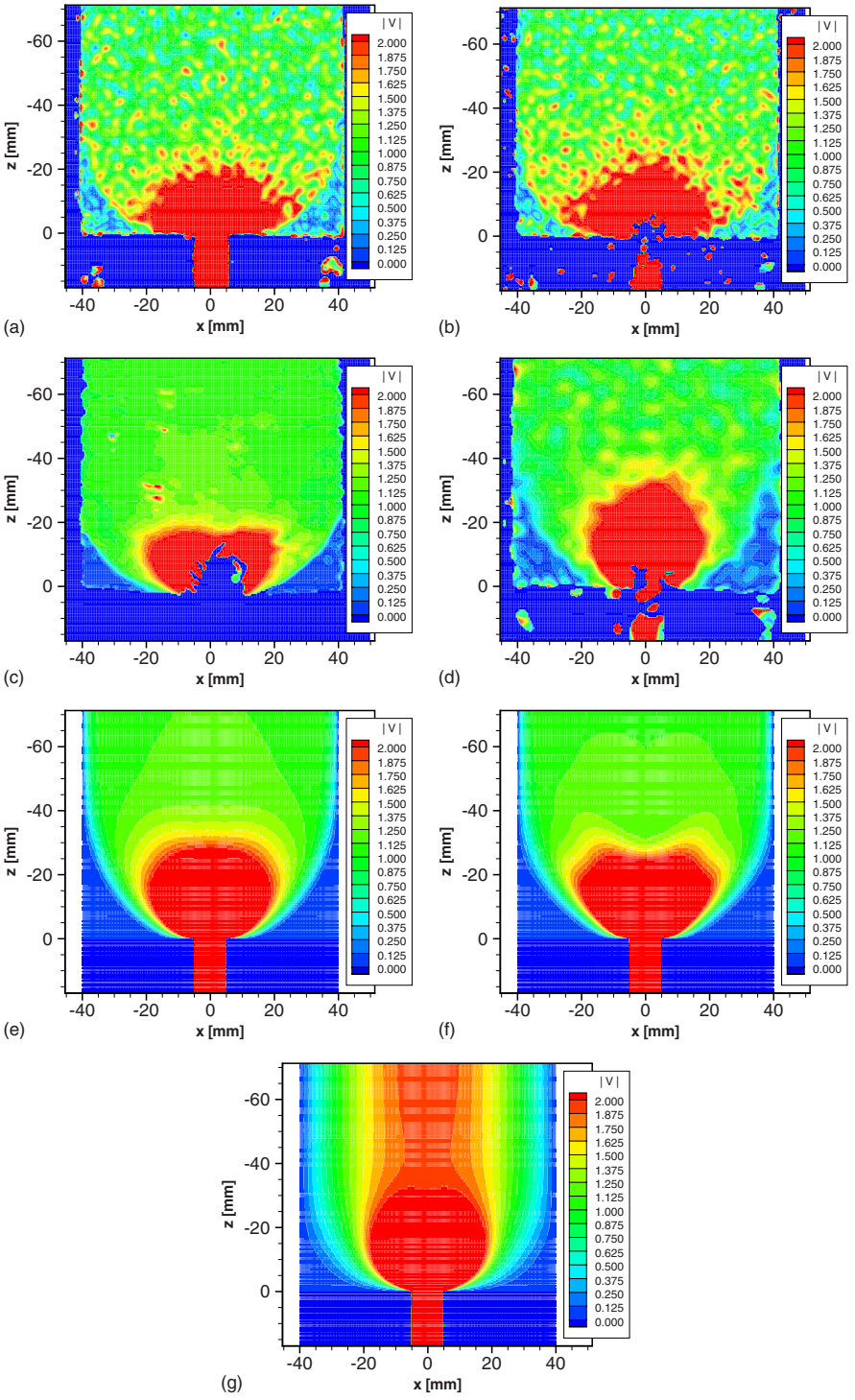

FIG. 4. (Color online) Typical velocity fields (given as the magnitude) during steady-state extrusion flows with different fluid types, with the velocity scaled by the piston velocity (0.2 mm/s). MRI measurements: (a) bentonite suspension, just after mixing; (b) bentonite suspension, after a long time of rest (18 h); (c) a Carbopol gel (see [28]), simple yield stress fluid; (d) a kaolin (clay) suspension in water, simple yield stress with possible solid migration leading to increase in the solid fraction in the dead zones. Our focus on the moderate velocities of the upper zone leads to signal loss in the high velocity regions near the die entrance, making the velocities measured inside the die, if present, irrelevant. Commercial software flow-3D simulations (see [28]): (e) simple yield stress fluid represented by a "biviscous" model (high viscosity below a critical shear rate), (f) simple yield stress fluid represented by a model including a true viscoelastic solid regime up to a critical deformation and a liquid regime behavior beyond this deformation, and (g) Newtonian fluid. Note that for the Newtonian fluid, in this dimensionless representation the velocity field is independent of the fluid viscosity. For the yield stress fluids the velocity field is almost constant for a Bingham number in the range 0.1–10 (the Bingham number is the ratio of the yield stress to the additional viscous part of the shear stress).

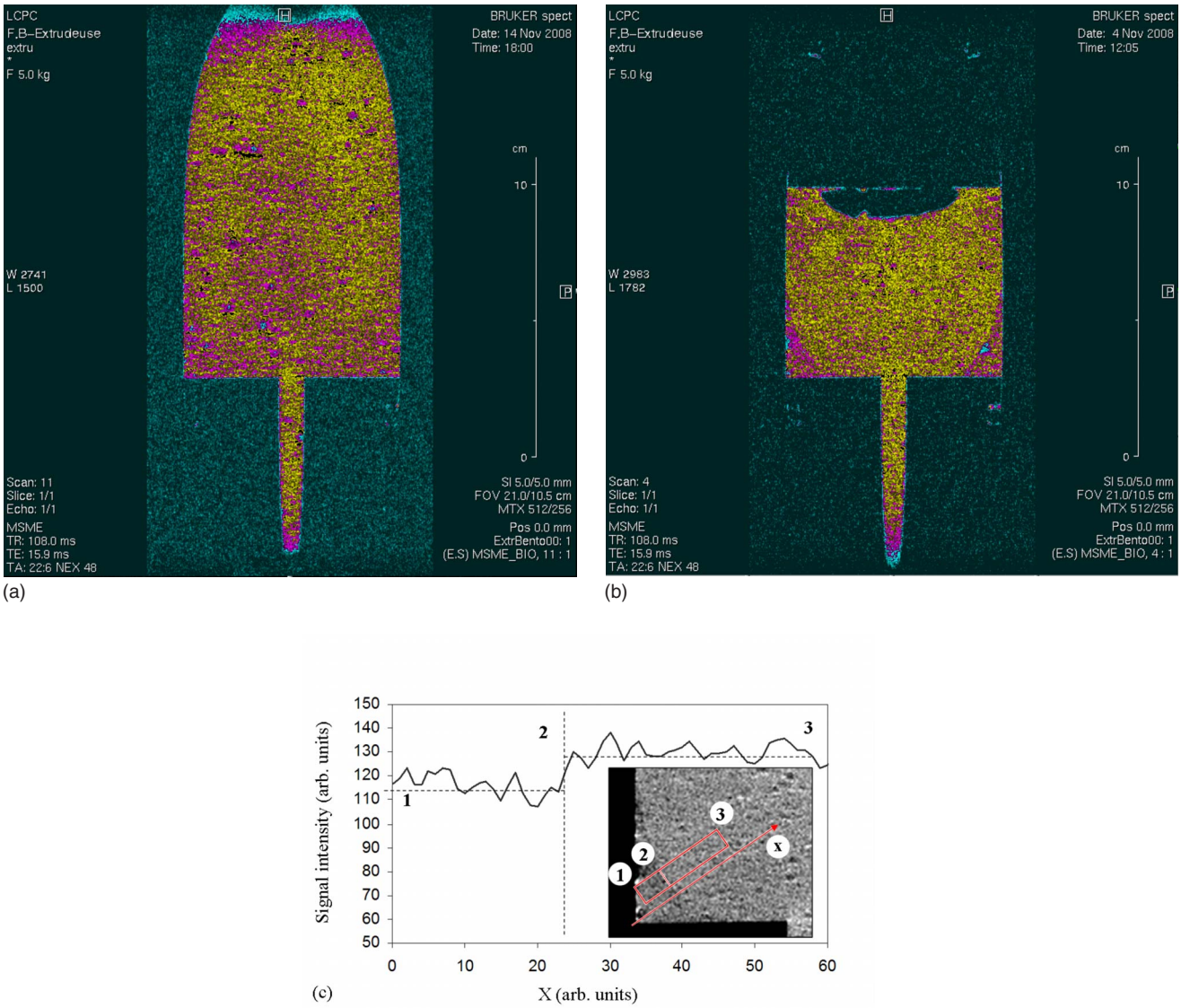

FIG. 5. (Color online) T_2-weighted images: (a) when the piston is far from the die and (b) when the piston is close to the die and after a flow following a rest of 18 h. The echo time allows optimal observation of T_2 variations. Dark (pink online) regions and image distortion at the very top and bottom of the pictures correspond to the edge of the imaging zone and should be disregarded. The image contrast here has been enhanced to highlight the 10% signal difference between the corners and the rest of the sample. Note that these are typical images extracted from a series of experiments with a similar procedure for setup and flow but with different timings for getting the MRI data and different sets of NMR coefficients but leading to consistent data. We finally obtained a quite consistent series of pictures from which we chose to present two typical ones. (c) Quantitative display of the evolution of signal intensity in the lower left corner of (b), as averaged along the indicated thick beam. Labels 1, 2, and 3 on the graphic correspond to labels 1, 2, and 3 on the beam. The vertical dashed line in the graphic corresponds to the dotted line drawn inside the beam and approximately indicates the boundary between dark (pink online) and light (yellow online) zones in (b). Horizontal dashed lines are a guide for the eyes and show a 10–15 % relative step in signal intensity at the boundary.

$$w_a \exp(-t/T_2^a) + w_b \exp(-t/T_2^b). \quad (9)$$

The majority of the water contained in the sample (over 99%) relaxes at the rate of T_2^a, whose value remains quite stable, around 11 ms, throughout the aging process (see Table I). The small variations that are observed—about 5% in relative value—cannot be clearly attributed to the aging process. It is possible that they could be simply a result of small variations in the room temperature. Moreover, when the sample is stirred again (rejuvenated) at the end of the experiment, T_2^a remains far from its initial value. It is clear that the T_2-weighted images are sensitive to T_2^a. Subsequently, we believe that the 10–15 % contrast in the image cannot be simply explained by the aging of the sample, but must instead involve a relative increase in the clay concentration of at least 10% in the corners of the extrusion setup.

More direct sensitivity to aging, however, may come from the T_2^b relaxing component. Although the very low w_b/w_a ratio means that it concerns a minor part of the sample, and although it is quite unusual in NMR studies to find such a

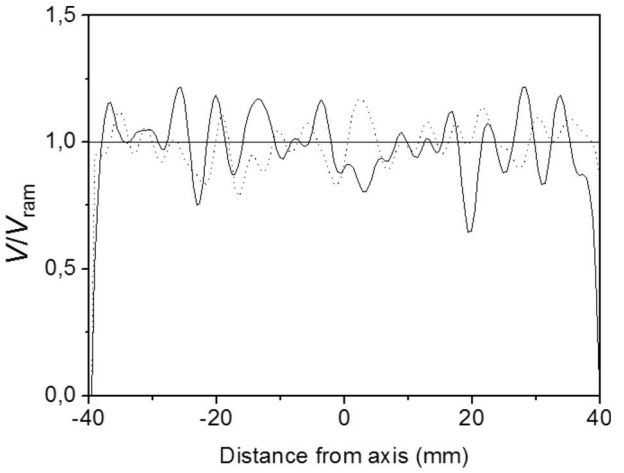

FIG. 6. Average flow profile of the vertical (z) velocity component vs the radial direction (x) in the two top centimeters of the flow data displayed in Figs. 4(a) and 4(b). Velocity values were scaled by their average value. For each curve, oscillations are on the same order of magnitude as those expected from the limited signal-to-noise ratio: (dotted line) just after mixing; (continuous line) after a 18 h rest.

stable part of signal at such a low level of intensity (about 100 ppm of the whole sample just after stirring), it exhibits significant and clear evolutions in time. Following the initial stirring, the amount of water related to T_2^b increases regularly by two orders of magnitude, reaching approximately 1% after a few days. Then, a new stirring of the sample returns it almost entirely to its initial state. The T_2^b values also undergo some variations throughout the aging process; however, globally they maintain relatively high values (a few hundred ms). In the context of the study of porous media, such long

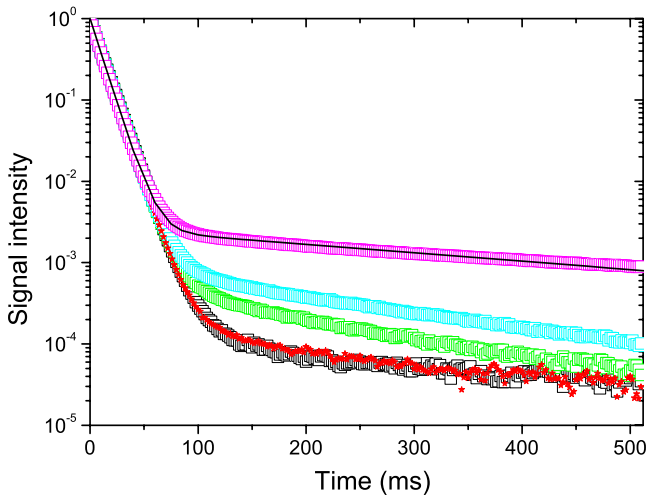

FIG. 7. (Color online) T_2 CPMG NMR signal decay (scaled by the value measured at the initial time) of a bentonite suspension (ϕ=5%) as a function of time. The curves are obtained for different times of rest after premixing. From bottom to top: from 0 to 1 h (black squares) and after 72 h at rest followed by a strong mixing (stars), after 8 h rest without mixing (light squares, green online), 16 h (light, blue online), 72 h (light squares, pink online). The continuous line shows an example of model fitting [Eq. (9)

TABLE I. Relaxation parameters of our bentonite suspension.

Material state	w_b/w_a	T_2^a (ms)	T_2^b (ms)
After 1 h at rest	0.00013	11.4	340
After 8 h at rest	0.00060	10.9	188
After 16 h at rest	0.00095	10.8	220
After 72 h at rest	0.0027	10.4	420
72 h rest sample remixed	0.00015	11	300

T_2^b values (few 100 ms)—as opposed to the short T_2^a values of the homogeneous paste (only 10 ms)—would be interpreted as the opening of large macropores in the material.

Within the frame of the eigenmode interpretation of NMR relaxation, we believe that the mode related to T_2^a, the mode responsible for more than 99.7% of NMR relaxation, is still the quasihomogeneous mode primarily controlled by the average suspension concentration. The long relaxing tail, however, shows that other eigenmodes exist, which could be a sign of microstructural arrangements developing within the bentonite paste.

Several different mechanisms can be used to explain the origin of these eigenmodes. The first mechanism is a progressive migration of water toward the wall of the container, creating a very thin layer of pure unconfined water. According to the 1D calculation of eigenmodes developed in the Appendix, T_2^b values close to 200 ms can be quantitatively explained by a layer thickness of about 30 μm. The surface area of our sample in the 1 l container used was approximately 600 cm^2. Such a layer, when fully developed, could then involve up to 2 cm^3 of water. This represents 0.2% of the entire sample, which is on the same order of magnitude as the long relaxing tail. Such a process, however, is unrealistic with our material: the bentonite suspension appears as a homogeneous gel (i.e., with no signs of apparent water migration) after most flow histories, including rests of several days. Moreover, we performed additional aging tests (not presented here), in which the bentonite suspension was placed in a series of small containers instead of a single large one, so as to increase the surface area of the sample. The long relaxing tail, however, was still present and, at the same amplitude, showing no correlation with the area of the external surface.

A second mechanism [see Fig. 8(a)] is the formation of cavities within the bentonite paste. They would result from local depletions in the clay particle concentration, opening pores containing, primarily, bulk water. According to the analysis performed in the Appendix—assuming a water cluster surrounded by clay paste—these pores would need to have a typical size of several tens of microns to explain the long relaxing tail in our CPMG experiments. However, from our understanding of the swelling behavior of bentonite suspensions, the opening of such large pores would be a very surprising result.

A more likely scenario is given in a third hypothesis [see Fig. 8(b)]. During aging, the evolution of the spatial distribution of clay platelets may randomly create cages within the

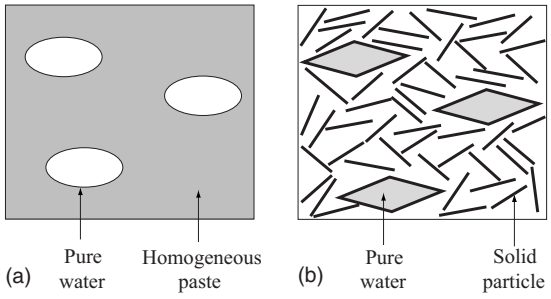

FIG. 8. Two scenarios possibly explaining the long relaxing tail in CPMG experiments: (a) spontaneous pore opening in the paste (unlikely) and (b) creation of cages between clay platelets, free of any paramagnetic impurity.

paste, entrapping small amounts of water. Unable to participate in diffusive exchange with the rest of the sample, this entrapped water may develop its own relaxation time. The relaxation kinetics of such boxes would be determined by the number of paramagnetic impurities in contact with the cage. One might imagine that, since the paramagnetic species are distributed randomly throughout the sample, some of the cages could be free of impurities, thus developing a longer relaxation time. In this way, the T_2^b relaxation time would then correspond to water entrapped in these long relaxing cages, while T_2^a would correspond to the average relaxation time in the rest of the sample.

These hypotheses of particle depletion and agglomeration, however, cannot be validated solely by NMR measurements. Moreover, beyond these simple models, the multiexponential relaxation may also be a clue as to the existence of more highly organized microstructures with which cannot be described simply as pores or as a modification in the local concentration of paramagnetic impurities. The corresponding T_2 value would instead reflect drastic local changes in the molecular dynamics with respect to the bulk behavior (see, e.g., [38]).

Finally, the "T_2^b tail" could simply indicate that a specific microstructure develops within the sample during aging. For example, one might expect the formation of a fractal aggregated structures tending to reinforce the strength of the structure but leading to a pore distribution with a larger amount of large pores and/or closed pores [42]. Stirring would simply destroy this structure, explaining the reversible characteristics of this relaxation component. Unfortunately, the T_2^b component, unlike the T_2^a component, involves too little water to be seen on the image during extrusion. This means that differences in the apparent density on the MRI images such as Fig. 5 are mainly due to some slight differences in the concentration even if significant aging differences can occur.

In general, the view we obtain from all of these results is summarized as follows. Aging and rejuvenation in bentonite paste are accompanied by microstructural changes which can be detected in NMR CPMG measurements. As far as NMR measurements are concerned, these changes appear to be reversible. However, differences in aging cannot be detected on MRI pictures of our extrusion setup since aging has no significant impact on the relaxation of the main liquid fraction in the sample. This conclusion is supported by the fact that there are no apparent density differences between the upper central regions of the fluid (far from the die) which is largely unperturbed and the regions close to the die which have been widely deformed. In contrast, the apparent difference between the corner regions and the rest of the fluid observed in Fig. 5 is likely due to a slight difference in the local concentration, about 10%, which progressively develops as a result of water filtration.

C. Analysis

Within the uncertainty of our data, the MRI velocity fields show that the vertical extent of the dead zones of our aging system is very similar to that of a simple yield stress fluid (see Fig. 4). This means that this dead region has a character intrinsic to a yield stress fluid, regardless of its specific characteristics in terms of constitutive equation and rheological parameters. The additional NMR results concerning the density and relaxation time suggest that these dead regions remain at rest whatever is the flow history, so that there can be a slight progressive density increase in these regions. This implies that we are dealing with genuine dead zones, which are distinctly separate from the flowing material, apart from a slight liquid migration.

Upon approach of the die, the flow accelerates, so that a flat rounded region of large velocities appears just along the die entrance. This strongly differs from the velocity field for most types of homogeneous viscous fluid [see Figs. 4(c)–4(g)]. In Newtonian or simple yield stress fluids, for example, the regions of large velocities take the form of a rounded zone separated from the bottom wall around the die entrance; thus, for these fluids there is a progressive transition between the (central) high velocity region and the very low velocity regions in the corners [see Figs. 4(c)–4(g)]. This progressive transition is typical of a homogeneous fluid flowing along a fixed surface. Roughly speaking, the progressive transition between the high and low velocity regions occurring during the extrusion process is due to the fact that the walls tend to retain the fluid, which thus flows more rapidly as one gets closer to the central axis.

For the bentonite suspension, the transition from the dead regions to the large velocity region is much more abrupt (see Fig. 9). In this context the clearest effect is that the velocity near the dead region is larger (by a factor about 2) than the piston velocity (approximately equal to the amplitude of the fluid velocity far above the die) (see Fig. 9). Thus, the velocity amplitude varies from an almost negligible value to twice the maximum value over a distance of approximately 5 mm, while this variation occurs over approximately 15 mm for a Newtonian or a yield stress fluid. Since the major behavioral difference between the bentonite suspension and the other fluids is its thixotropic character, it is suggested that this effect is at the origin of the strong differences in the characteristics of this extrusion flow. More specifically we believe that this effect is due to the ability of the material's viscosity to evolve differently, depending on the flow history.

In this context the largest velocities observed for an aging material close to the dead regions are likely due to a fluid viscosity lower in these regions than along the central axis.

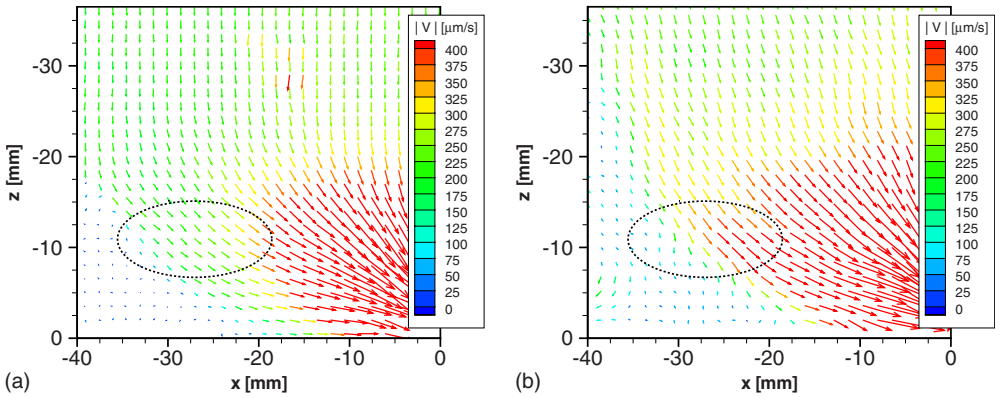

FIG. 9. (Color online) The experimental steady-state flow field in the upper zone and left side of an 8:1 contraction with an imposed piston velocity of 200 μm/s displaying the corresponding vector field of the lower left corner: (a) for a simple yield stress fluid (Carbopol gel [28]) and (b) for a bentonite suspension. The dotted elliptical line focuses on the same specific zone.

This necessarily results from a higher rejuvenation in the lateral regions and leads to an effect reminiscent of shear banding in uniform flows: although the viscosity far from the die is homogeneous it takes different values at the approach of the die depending on the streamline considered; the viscosity decreases more along a path close to the dead region than along the central axis. The viscosity thus follows some specific path of evolution along each streamline.

In this respect it is surprising that the velocity fields are similar within the uncertainty of our data after different times of rest [see Figs. 5(a) and 5(b)]. This suggests that these paths exhibit some similarities; even if the initial apparent viscosity is significantly different, the relative variations of the viscosity of the material along each path are similar.

IV. SQUEEZE FLOW EXPERIMENTS

To check this we carried out squeeze tests, i.e., flows of the material between two parallel plates approaching each other, which makes the material undergo a deformation with some global analogy with that undergone during extrusion: the sample shape is initially a cylinder with a height on the same order of its radius and ends with a much thinner thickness. In such tests it is nevertheless possible to measure the force effectively applied to the material without the possible problems encountered in extrusion. The setup was described in detail in [43]. The procedure consisted of squeezing a fixed volume of the sample (1 ml) between two rough plates down to a given distance of separation, namely, $h_0 = 2.16$ mm, then stopping the motion and leaving the material at rest for a given time. After the specified resting time the test continued with a further approach at a given velocity. The force at rest differs from zero: initially it corresponds to the force needed to squeeze the material down to h_0, but as the material ages the stresses relax and we could observe that with these bentonite suspensions the residual force just before starting a test had decreased to a negligible value. We then recorded the force (F) vs distance (h) data during the plate displacement motion for $h < h_0$. The apparent deformation of the sample may be defined as $\varepsilon = (h_0 - h)/h$. For $h \approx h_0$ this corresponds to the usual definition of the deformation; when h is significantly different from h_0 this is only some global deformation amount which is described via ε since the deformation is likely strongly heterogeneous.

The force increases rapidly at low deformation (see Fig. 10), which likely corresponds to the viscoelastic solid regime, then it reaches a plateau likely associated with the solid-liquid transition, and finally increases significantly. The aspect of the curves obtained after different times of rest is similar, so that they can be scaled vertically by a factor increasing with the time of rest to obtain a single master curve. This shows that the material likely undergoes a similar deformation history and only the force changes by a single factor. Once again this means that starting from different times of rest the material follows a similar path of changes in its structure. More precisely we expect a kind of cascade of floc breakage into smaller sizes as flow advances; these cascades are essentially governed by the deformation imposed, and thus are geometrically similar for a given deformation history. The corresponding force needed to impose this deformation always follows the same variation by a factor depending on the initial strength of the material.

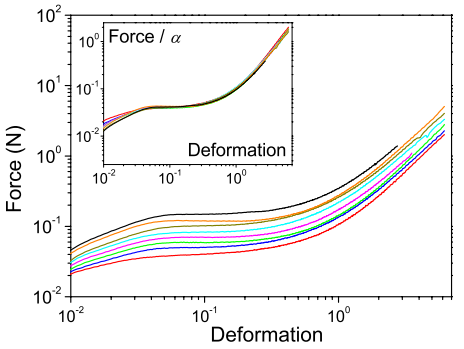

FIG. 10. (Color online) Force vs apparent deformation (see text) for squeeze flows (at a velocity of mm/s) with the bentonite suspension after different times of rest: (from bottom to top) 0, 3, 10, 20, 30, 60, 90, and 180 min. Inset: same data with the force scaled by a factor (see values in the main panel) depending on the time of rest.

V. DISCUSSION

So far the rejuvenation of soft-jammed systems has been essentially dealt with when studying the viscosity decrease in time of thixotropic materials. The knowledge of the underlying mechanisms however remains poor: one may observe some similarities in the viscosity decrease in time well described by an exponential law [6], but the usual theoretical description involves a viscosity depending on a structure parameter, which varies according to some kinetic equation [44]. A very simple phenomenological model of that type [9,45] has been provided for describing the major flow trends observed with aging soft-jammed systems. It appears to be able to explain the present results. In simple shear the apparent viscosity (η) of the fluid is a function of the actual state of structure λ, which may represent the number of flocs, via $\eta=\eta_0(1+\lambda^n)$, in which η_0 and n (>1) are two material parameters. The aging character of the fluid finds its origin in the time variations of λ, which results from the competition between the restructuring and the destructuring processes: $d\lambda/dt=1/\theta-\alpha\lambda\dot{\gamma}$, in which θ is the characteristic time of restructuration and $\dot{\gamma}$ is the shear rate. Here, we are dealing with a material which is significantly aged before flow starts, so that we assume $\lambda \gg 1$. Also we focus on the initial stage of the solid-liquid transition, which mainly involves the destructuring processes, leading one to neglect $1/\theta$ in the kinetic equation. In this context the relative rate of decrease in the number of flocs ($d\lambda/\lambda$) over a short time dt, is simply proportional to the deformation imposed ($\dot{\gamma}dt$). If the initial state is λ_0 we find $\lambda(t)=\lambda_0\exp(-\alpha\gamma)$, in which γ is the total deformation at t, and $\eta/\eta(0)=\exp(-n\alpha\gamma)$, in which $\eta(0)=\eta_0\lambda_0^n$ is the viscosity at the initial time. Thus, this model predicts that the ratio of the current to the initial viscosity is a function depending solely on the deformation undergone by the material. This approach can be generalized to a 3D flow with the help of a 3D Newtonian constitutive equation with the apparent viscosity following the same type of evolution using the strain rate tensor instead of the shear rate.

Let us now consider a "flow problem," defined as the detailed flow characteristics obtained for given geometric and kinematic boundary conditions. For a material behavior as described above, if we have found the solution to a given flow problem for some specific initial state, we have the solution for any other initial state by using the same velocity field and a stress distribution increased by a constant factor equal to the ratio of the initial viscosities. Thus, the solutions to the flow problem for different initial states—but with the same boundary conditions—are the same in terms of the velocity field. This result may be applied to our extrusion and squeeze flow tests: the flow geometry is well defined and the kinematics along the boundary is imposed by the piston or plate motion. Thus, our model is able to explain the similarities observed, which suggest that the physical assumptions behind the model are valid.

In this context we can also expect that the force factor which governs the impact of rest on any flow type varies in a similar way for different flow types: we observe that this is effectively the case for simple shear and squeezing (see Fig. 11). In this figure we also show that the shear elastic modulus (measured with the help of the Couette system) varies in a similar way.

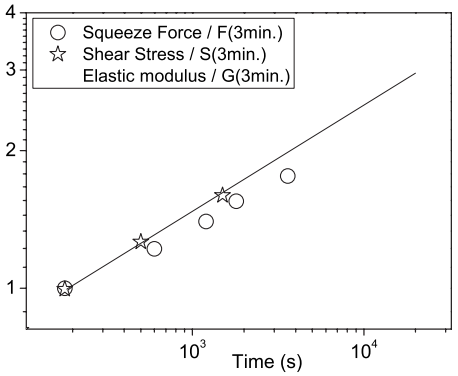

FIG. 11. Scaling factors as a function of time of rest. Squeeze flow: factor used to rescale the curves of Fig. 10 and obtain the master curve in the inset (using a factor of 1 for 3 min of rest). Simple shear: same approach for obtaining the master curve in the inset of Fig. 1. Elastic modulus: ratio of the elastic modulus to its value after 3 min of rest.

Aside from this, we also observe (see Figs. 12 and 13) that these processes are influenced by the rate at which the deformation is imposed, suggesting that there are some viscous effects. In fact the corresponding curves of shear stress vs deformation for the squeeze or simple shear are simply shifted by a similar factor along the two axes (see insets of Figs. 12 and 13). This means that all occurs as if there is an additional deformation induced by a faster deformation, inducing a larger stress by the same factor. However, it is worth emphasizing that the shear elastic modulus, which is related to the position of the line of slope 1 along the data at low deformation in this logarithmic representation, remains constant whatever is the shear rate (see Fig. 12). Note that these effects correspond to viscoelastic effects which are not encompassed by the above simple model.

A natural explanation in this frame is that the macroscopic deformation induces the formation of blobs or flocs of

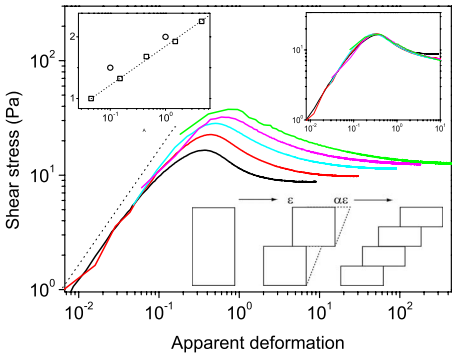

FIG. 12. (Color online) Shear stress vs apparent deformation for creep tests described in Fig. 1, but for different apparent shear rates (after a time of rest of 10 min following preshear): (from bottom to top) 0.045, 0.15, 0.45, 1.5, and 4.5 1/s. Insets: (top right) same data scaled vertically and horizontally by the same factor depending on the time of rest; (top left) force factor as a function of the shear rate (squares), as a function of the vertical velocity (in mm) for the squeeze tests shown in Fig. 11 (circles); (bottom) conceptual view of the destructuration process, depending only on the imposed deformation and relying on breakage and deformation of flocs.

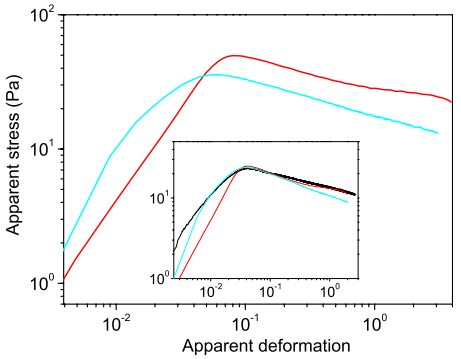

FIG. 13. (Color online) Apparent shear stress vs apparent deformation for squeeze tests described in Fig. 4 for a time of rest of 10 min, but for different vertical velocities: (from bottom to top) 0.01, 0.1, and 1 mm/s. Insets: (top) same data scaled vertically and horizontally by the same factor depending on the time of rest. Here, we computed the apparent shear stress from the vertical force via $\tau = 3Fh/2\pi R^3$, in which R is the current radius of the squeezed layer; this relation is derived from the usual expression for the critical squeezing force under the lubrication assumption [2].

smaller and smaller sizes as the deformation progresses, but additionally these flocs may temporarily be slightly more deformed (see the inset of Fig. 12). These additional deformations then relax even more if the relaxation time (say θ_0) of the elastic flocs is smaller than the characteristic time of flow (typically $1/\dot{\gamma}$). This explains why on average the additional deformation is larger for larger $\dot{\gamma}$. Moreover, we emphasize that this additional transient deformation is likely related to the same physical effects as for the floc breakages and deformations leading to the basic macroscopic deformation (at a negligibly low rate): in all these situations the source of energy dissipation or storage is the relative displacements of the particles in colloidal interaction.

Thus, we can expect that the force needed to maintain some average additional deformation will be in the same proportion as the basic force function of the basic deformation. In other words, if the force for a given rate of deformation ε is expressed as the function $F(\varepsilon)$, the force function for an additional transient deformation by a factor α can be expressed as $F^*(\alpha\varepsilon) = \alpha F(\varepsilon)$. This explains the scaling in the insets of Figs. 12 and 13. It is remarkable that the force factor is exactly proportional to the logarithm of the shear rate (see the inset of Fig. 12); however, we have no physical explanation for this. We believe that further developments in the methodology, such as the local ultrasonic measurements used in [12] or the "long relaxing tail" observed here in our NMR CPMG experiments, may open the way toward a better understanding of those microstructural phenomena.

VI. CONCLUSION

These results show that the viscosity paths followed by a material during the solid to liquid transition under the same deformation history are similar by a factor associated with its initial state. Our additional results concerning the impact of the rate at which the deformation is imposed suggests that during this transition the state of the material may be described by a single parameter reflecting the average size and deformation of the flocs. Spin-spin NMR relaxation measurements showed a clear sensitivity to microstructural changes in a bentonite sample and, in the future, may lead to a better understanding of the nature and kinetics of phenomenon associated with aging-rejuvenation cycles. These results also show that some localization of flow occurs only as a result of a progressive differential evolution of the material in different regions of the flow, and thus are basically associated with the specific boundary conditions of the flow. In particular shear banding needs a uniform flow to develop, in other words a flow with similar characteristics along a given direction over a significant distance. This suggests that further information on the aging characteristics of soft-jammed systems may be obtained from a systematic scaling analysis of flows with complex boundary conditions.

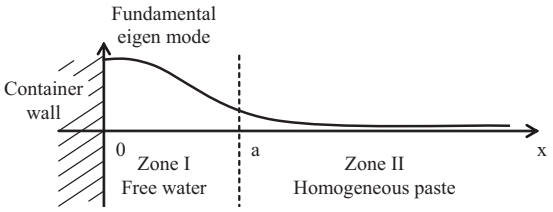

FIG. 14. 1D model for localized relaxation eigenmodes in a water layer surrounding the bentonite clay. The bold curve shows the approximate shape of the fundamental relaxation mode involved in CPMG measurements.

ACKNOWLEDGMENT

The authors acknowledge financial support of ANR for this work, within the frame of project PHYSEPAT Contract No. ANR-05-BLAN-0131.

APPENDIX: 1D MODEL FOR RELAXATION IN A THIN LAYER OF WATER ON THE CONTAINER WALL

The idea of this model is to test quantitatively how water migration toward the surface of the container (aging experiments reported in Sec. III B) might explain the appearance of new relaxation modes in the bentonite sample. It can also be used to obtain quantitative estimates of a typical pore size for the (second) hypothesis of spontaneous pore opening. The sample at the vicinity of the interface is described as follows (see Fig. 14).

Zone I: a layer of pure water. Let a be its thickness. No significant relaxation process is assumed to occur on the container wall. Following the ideas of Brownstein and Tarr, the time evolution of the local NMR signal density $s(x,t)$ during proton spin-spin relaxation is modeled as

$$\frac{\partial s}{\partial t} = D\frac{\partial^2 s}{\partial x^2} - \frac{s}{T_b} \quad \text{for } 0 < x < a,$$

$$\frac{\partial s}{\partial x}(x=0) = 0, \tag{A1}$$

where $D = 2 \times 10^{-9}$ m^2 s^{-1} is the self-diffusion coefficient of water molecules and $T_b = 3$ s is the spin-spin relaxation time

of pure water in our working conditions (20 °C, 0.5 T).

Zone II: an infinitely thick layer of homogeneous bentonite paste. Due to the low volume concentration of clay particles, the porosity of the paste is taken to be 100%. The local NMR signal density $s(x,t)$ is assumed to obey the law

$$\frac{\partial s}{\partial t} = D\frac{\partial^2 s}{\partial x^2} - \frac{s}{T_p} \quad \text{for } x > a, \tag{A2}$$

where the self-diffusion coefficient of water molecules in the paste is taken to be the same as in bulk water. This is done since only very high clay concentrations associated with nematic ordering of clay particles have previously been shown to induce noticeable modifications [29,30]. $T_p = 10$ ms is the spin-spin relaxation time inside the homogeneous paste.

Boundary conditions between zones I and II are standard conditions for a diffusive process,

$$s(a^+) = s(a^-), \quad \frac{\partial s}{\partial x}(a^+) = \frac{\partial s}{\partial x}(a^-). \tag{A3}$$

In this system, relaxation eigenmodes are defined by functions $\varphi(x)$ and times T which follow

$$-\frac{1}{T}\varphi = D\frac{\partial^2 \varphi}{\partial x^2} - \frac{\varphi}{T_b} \quad \text{for } 0 < x < a,$$

$$-\frac{1}{T}\varphi = D\frac{\partial^2 \varphi}{\partial x^2} - \frac{\varphi}{T_p} \quad \text{for } x > a. \tag{A4}$$

These also fulfill the boundary conditions of Eqs. (A1) and (A3). The practical determination of eigenmodes in this situation turns out to be very similar to standard problems in quantum mechanics. We refer to textbooks on the subject for the more technical aspects [46].

The general solution for so-called "linked eigenstates" reads

$$\varphi(x) = \cos(kx) \quad \text{for } 0 < x < a,$$

$$\varphi(x) = \cos(ka)\exp[-K(x-a)] \quad \text{for } x > a, \tag{A5}$$

where k and K are real positive coefficients related to the eigen-relaxation-time T following

$$\frac{1}{T} = Dk^2 + \frac{1}{T_b} = -DK^2 + \frac{1}{T_p},$$

$$K = k\tan(ka). \tag{A6}$$

This system has only a finite number of solutions. There is always one and only one solution with $0 < k < \pi/2a$. This solution corresponds to the fundamental mode, that is, the one with the longest relaxation time, and is usually the most visible mode in an NMR relaxation experiment. The typical shape of this eigenmode is shown in Fig. 14. It describes a relaxation process localized in the vicinity of the water layer.

A study of the system of equations in Eq. (A6) shows that the fundamental relaxation time is a growing function of the water thickness a. This has been verified numerically for our working conditions, equaling 200 ms for $a \approx 30$ μm.

[1] A. J. Liu and S. R. Nagel, Nature (London) **396**, 21 (1998).
[2] P. Coussot, *Rheometry of Pastes, Suspensions and Granular Materials* (Wiley, New York, 2005).
[3] L. C. E. Struik, *Physical Aging in Amorphous Polymers and Other Materials* (Elsevier, Houston, TX, 1978).
[4] C. Derec *et al.*, C. R. Acad. Sci., Ser IV: Phys., Astrophys. **1**, 1115 (2000); M. Cloitre, R. Borrega, and L. Leibler, Phys. Rev. Lett. **85**, 4819 (2000); G. Ovarlez and P. Coussot, Phys. Rev. E **76**, 011406 (2007); Y. M. Joshi and G. R. K. Reddy, *ibid.* **77**, 021501 (2008); Y. M. Joshi *et al.*, Proc. R. Soc. London, Ser. A **464**, 469 (2008).
[5] P. Coussot *et al.*, J. Rheol. **50**, 975 (2006).
[6] K. Dullaert and J. Mewis, J. Non-Newtonian Fluid Mech. **139**, 21 (2006).
[7] P. Coussot, Soft Matter **3**, 528 (2007).
[8] F. Pignon, A. Magnin, and J. M. Piau, J. Rheol. **40**, 573 (1996); P. Coussot *et al.*, Phys. Rev. Lett. **88**, 218301 (2002).
[9] P. Coussot *et al.*, Phys. Rev. Lett. **88**, 175501 (2002).
[10] A. Ragouilliaux *et al.*, Phys. Rev. E **76**, 051408 (2007).
[11] G. Ovarlez *et al.*, Rheol. Acta **48**, 831 (2009).
[12] T. Gibaud *et al.*, Soft Matter **5**, 3026 (2009).
[13] P. T. Callaghan, *Principles of Nuclear Magnetic Resonance Microscopy* (Oxford University Press, New York, 1991).
[14] A. D. S. Hanlon *et al.*, Magn. Reson. Imaging **16**, 953 (1998).
[15] P. T. Callaghan, Rep. Prog. Phys. **62**, 599 (1999).
[16] J. Götz *et al.*, J. Non-Newtonian Fluid Mech. **98**, 117 (2001); K. G. Hollingsworth and M. L. Johns, J. Rheol. **48**, 787 (2004); G. Ovarlez *et al.*, Phys. Rev. E **78**, 036307 (2008).
[17] J. S. Raynaud *et al.*, J. Rheol. **46**, 709 (2002).
[18] H. D. Siebert *et al.*, Rheol. Acta **36**, 618 (1997).
[19] S. Jarny *et al.*, Cem. Concr. Res. **35**, 1873 (2005).
[20] S. Rodts *et al.*, EPL **69**, 636 (2005).
[21] P. Møller *et al.*, Phys. Rev. E **77**, 041507 (2008).
[22] C. K. Agemura *et al.*, J. Food. Eng. **25**, 55 (1995).
[23] M. H. G. Amin *et al.*, Meas. Sci. Technol. **14**, 1760 (2003).
[24] S. Rodts *et al.*, C. R. Chim. **7**, 275 (2004).
[25] J. Götz *et al.*, Rheol. Acta **41**, 134 (2002).
[26] J. Götz *et al.*, Chem. Eng. Process. **42**, 517 (2003).
[27] E. C. Barnes, D. I. Wilson, and M. L. Johns, Chem. Eng. Sci. **61**, 1357 (2006).
[28] B. D. Rabideau *et al.*, J. Non-Newtonian Fluid Mech. (to be published).
[29] P. Porion *et al.*, Phys. Rev. Lett. **87**, 208302 (2001).
[30] P. Porion *et al.*, J. Phys. Chem. B **107**, 4012 (2003).
[31] S. V. Dvinskikh *et al.*, J. Magn. Reson. **198**, 146 (2009).
[32] P. Coussot and F. Gaulard, Phys. Rev. E **72**, 031409 (2005).
[33] S. Stapf and S. Han, *NMR Imaging in Chemical Engineering* (Wiley-VCH, New York, 2006).

[34] A. Abragam, *The Principles of Nuclear Magnetism* (Clarendon Press, Oxford, 1961).
[35] H. Y. Carr and E. M. Purcell, Phys. Rev. **94**, 630 (1954).
[36] P. Le Doussal and P. N. Sen, Phys. Rev. B **46**, 3465 (1992).
[37] K. R. Brownstein and C. E. Tarr, J. Magn. Reson. **26**, 17 (1977); Phys. Rev. A **19**, 2446 (1979).
[38] P. F. Faure and S. Rodts, Magn. Reson. Imaging **26**, 1183 (2008).
[39] S. Godefroy *et al.*, Phys. Rev. E **64**, 021605 (2001).
[40] T. H. Ohkubo *et al.*, Phys. Chem. Earth **33**, S169 (2008).
[41] S. Meiboom and D. Gill, Rev. Sci. Instrum. **29**, 688 (1958).
[42] S. Reynaert, P. Moldenaers, and J. Vermant, Langmuir **22**, 4936 (2006).
[43] B. D. Rabideau, C. Lanos, and P. Coussot, Rheol. Acta **48**, 517 (2009).
[44] J. Mewis and N. J. Wagner, Adv. Colloid Interface Sci. **147-148**, 214 (2009).
[45] N. Roussel, R. Le Roy, and P. Coussot, J. Non-Newtonian Fluid Mech. **117**, 85 (2004).
[46] J. L. Basdevant and J. Dalibard, *Mécanique Quantique* (Editions Ellipse, Paris, 2001).